

Simulating the Universe with MICE : The abundance of massive clusters

Martín Crocce, Pablo Fosalba, Francisco J. Castander & Enrique Gaztañaga

Institut de Ciències de l'Espai, IEEC-CSIC, Campus UAB, Facultat de Ciències, Torre C5 par-2, Barcelona 08193, Spain

24 October 2018

ABSTRACT

We introduce a new set of large N-body runs, the MICE simulations, that provide a unique combination of very large cosmological volumes with good mass resolution. They follow the gravitational evolution of ~ 8.5 billion particles (2048^3) in volumes covering up to ~ 15 Hubble volumes (i.e., $450 h^{-3} \text{Gpc}^3$), and sample over 5 decades in spatial resolution. Our main goal is to accurately model and calibrate basic cosmological probes that will be used by upcoming astronomical surveys of unprecedented volume. Here we take advantage of the very large volumes of MICE to make a robust sampling of the high-mass tail of the halo mass function (MF). We discuss and avoid possible systematic effects in our study, and do a detailed analysis of different error estimators. We find that available fits to the local abundance of halos (Warren et al. (2006)) match well the abundance estimated in the large volume of MICE up to $M \sim 10^{14} h^{-1} M_\odot$, but significantly deviate for larger masses, underestimating the mass function by 10% (30%) at $M = 3.16 \times 10^{14} h^{-1} M_\odot$ ($10^{15} h^{-1} M_\odot$). Similarly, the widely used Sheth & Tormen (1999) fit, if extrapolated to high redshift assuming universality, leads to an underestimation of the cluster abundance by 30%, 20% and 15% at $z = 0, 0.5, 1$ for fixed $\nu = \delta_c/\sigma \approx 3$ (corresponding to $M \sim [7 - 2.5 - 0.8] \times 10^{14} h^{-1} M_\odot$ respectively). We provide a re-calibration of the MF over 5 orders of magnitude in mass ($10^{10} < M/(h^{-1} M_\odot) < 10^{15}$), that accurately describes its redshift evolution up to $z = 1$. We explore the impact of this re-calibration on the determination of the dark-energy equation of state w , and conclude that using available fits that assume universal evolution for the cluster MF may systematically bias the estimate of w by as much as 50% for medium-depth ($z \lesssim 1$) surveys. The halo catalogues used in this analysis are publicly available at the MICE webpage, <http://www.ice.cat/mice>.

1 INTRODUCTION

Near future extra-galactic surveys will sample unprecedentedly large cosmological volumes, in the order of tens of cubic gigaparsecs, by combining wide fields with deep spectroscopy or photometry, typically reaching $z \sim 1$ (e.g. DES, PAU, BOSS, PanSTARRS, WiggleZ¹). In addition they will be able to capture very faint objects and lower their shot-noise level to become close to sampling variance limited. Optimizing the preparation and scientific exploitation of these upcoming large surveys requires accurate modeling and simulation of the expected huge volume of high quality data. This is quite a non-trivial task, because it involves simulat-

ing a wide dynamic range of cosmological distances in order to accurately sample the large-scale structure, and well resolved dark-matter halos as a proxy to galaxy clusters, to model the physics of galaxy formation and other nonlinear physics.

Over the past decades numerical simulations have provided one of the most valuable tools to address these issues, and their relevance will certainly increase in the near future. They allow to follow the growth of cosmological structure, shed light on the process of galaxy formation, model nonlinear effects entering different clustering measures, lensing and redshift distortions, track the impact of a dark-energy component and more. Among projects related to the development of very large-simulations are those carried out by the Virgo consortium (Frenk et al. 2000), the Millennium I and II (Springel et al. 2005; Boylan-Kolchin et al. 2009), the Horizon run (Kim et al. 2008) and the Horizon project (Teyssier et al. 2009). They have all benefited by the vast

¹ DES (<http://www.darkenergysurvey.org/>); PAU (<http://www.ice.csic.es/pau/Survey.html>); BOSS (<http://cosmology.lbl.gov/BOSS/>); PanSTARRS (<http://pan-starrs.ifa.hawaii.edu>); WiggleZ (<http://wigglez.swin.edu.au/>)

computational power and hardware developed over the past years.

In this paper we present a new effort to tackle the demand of large simulations and mock catalogues, the MareNostrum Institut de Ciències de l’Espai (MICE) simulations, that aims at the development of very large and comprehensive N-body runs to deliver an unprecedented combination of large simulated volumes with good mass resolution.

As a first step, we have developed two N-Body simulations including more than 8 billion particles (2048^3) each, in volumes similar and well beyond the one corresponding to the Hubble length ($\sim 30 h^{-3} \text{Gpc}^3$), in addition to several other large runs of typically smaller volume and corresponding higher mass resolution that are complementary to the large volume runs.

Some of the MICE simulations used in this paper have already been used to develop the first full-sky weak-lensing maps in the lightcone (Fosalba et al. 2008), or study the clustering of LRG galaxies with multiple-band photometric surveys such as PAU (Benitez et al. 2009). More recently, using the largest volume simulations, a series of papers has studied the large-scale clustering in the spectroscopic LRG SDSS sample, through the redshift space distortions (Cabr e & Gazta naga 2009a; Cabr e & Gazta naga 2009b), the baryon oscillations in the 3-point function (Gazta naga et al. 2008a), and in the radial direction (Gazta naga et al. 2008b).

In this paper we will focus on the mass function of the most massive objects formed through hierarchical clustering, since their low abundance makes the need of large sampling regions crucial. In turn, a precise description of this regime is of paramount importance since the abundance of clusters, to which it corresponds to, is very sensitive to cosmological parameters (particularly the matter density), the normalization of the matter power spectrum and the expansion history of the universe, characterized by the dark energy density and its equation of state (e.g. see Rozo et al. 2009; Cunha 2009; Mantz et al. 2008; Henry et al. 2009; Vikhlinin et al. 2009 and references therein). This regime is also one of the best probes to search for primordial non-Gaussianities (e.g. Matarrese et al. 2000; Grossi et al. 2007; Pillepich et al. 2008; Maggiore & Riotto 2009)

The halo mass function and related topics have been extensively studied in the literature. Analytic models predicting not only the abundance as a function of mass but also the evolution were developed as far back as the 70’s by (Press & Schechter 1974) and followed by (Bond et al. 1991; Lee & Shandarin 1998; Sheth et al. 2001). However the development of N-body simulations showed that these predictions were in general not sufficiently accurate for cosmological applications, and demanded the need for calibrations against numerical results (see also Robertson et al. 2009). Although N-body studies were likewise early developed (e.g. two 1000 particles simulation by Press & Schechter 1974), the reference work in this directions was set by (Sheth & Tormen 1999) and (Jenkins et al. 2001). More recent re-calibrations of the mass function to within few percent were put forward by (Warren et al. 2006; Tinker et al. 2008). In addition these or other papers have focused

their attention on the redshift evolution of the mass function (Reed et al. 2003; Reed et al. 2006; Lukic et al. 2007; Cohn & White 2007), different definitions of halo and halo mass (White 2001; White 2002; Tinker et al. 2008) or the impact of gas physics associated with halo baryons (Stanek et al. 2009a).

In this paper we combine the effect of long-wavelength modes whose contribution can only be studied with the unprecedented volume of the MICE simulations ($\sim 30, 100$ and $450 h^{-3} \text{Gpc}^3$), with good mass resolution and controlled systematics to investigate how well available fits describe the high-mass end tail of the halo mass function. We complement this with a nested-volume approach of N-body runs to probe smaller masses in a way to sample the mass function over 5 decades in mass.

Before proceeding we recall that in hierarchical models of structure formation, as our present cosmological paradigm, halos are often found merging or accreting rather than isolated, and therefore have no definite boundary. Hence defining a halo and its mass becomes rather conventional.

There are two widely used conventions. The spherical overdensity (SO, Lacey & Cole 1994) halos are defined as spherical regions around matter density peaks with an inner density larger than a given threshold, which is generally taken as a fixed multiple of the critical or background density. Alternatively, the Friends-of-Friends (FoF, Davis et al. 1985) algorithm identifies all the neighbors to a given particle separated by less than a fixed distance (the linking length). The same algorithm is then applied to each neighbor recursively until no more “friends” are found. The end result is a group of particles in space whose boundary approximately matches an iso-density contour (e.g. see Fig 1 in Lukic et al. 2009).

Each definition has advantages and disadvantages, and the overall convenience of one over the other is currently an open debate (Jenkins et al. 2001; White 2002; Tinker et al. 2008; Lukic et al. 2009). The abundance of FoF halos has been found universal at $< 10\%$ level by different studies including ourselves in Sec. 8 (Jenkins et al. 2001; Reed et al. 2003; Heitmann et al. 2006; Reed et al. 2006; Lukic et al. 2007; Tinker et al. 2008), with some dependence on the linking length (Jenkins et al. 2001; Tinker et al. 2008). Given the complicated non-linear processes that drive halo formation, having a universal mass-function (i.e. independent of red-shift and cosmology) at this level could be very convenient alleviating the need to simulate individual cosmologies. In contrast, the abundance of SO halos is considerably less universal, showing evolution in the halo mass function amplitude at the level of $20\% - 50\%$, depending on cosmology, but also evidence for red-shift dependence of its overall shape (Tinker et al. 2008). The current error budget of cluster science is dominated by the unknowns in the calibration of mean and scatter of the mass-observable relations (e.g. Voit 2005; Rozo et al. 2009; Stanek et al. 2009b). Only after understanding these better we will be able to state what is an acceptable degree of non-universality in future precision cosmology (but see also Stanek et al. 2009a).

In turn, the general idea of defining virialized structure

and mass in terms of spherical apertures is more directly linked to observations of galaxy groups and clusters (e.g. Voit 2005), in part because the scaling correlations between cluster observable and mass are tighter in this approach. Nonetheless, relating iso-density methods such as FoF is also possible (e.g. Eke et al. 2006; Tago et al. 2008; Wen et al. 2009).

For concreteness, we will next focus on FoF halos and leave SO for a follow-up study, although we have tested to some extent that our main results are robust in front of this choice, as we further discuss in our Conclusions.

This paper is organized as follows: In Sec. 2 we describe the MICE simulations. Sec. 3 recaps known theoretical predictions and fits to the halo mass function and concludes with a comparison between MICE and results from previous simulations. In Sec. 4 we discuss systematic effects that are most relevant in the measurement of the high-mass end of the mass function, such as transients from initial conditions, finite sampling of the mass distribution, and mass resolution effects. A detailed error analysis including different estimators is provided in Sec. 6, whereas in Sec. 7 we derive a new fitting function to account for the high-mass tail of the halo mass function. The higher redshift evolution, including results regarding mass function universality, is the subject of Sec. 8. We discuss the implications of our results for dark-energy constraints in Sec.9, and we finish by summarizing and discussing our main findings in Sec. 10.

2 THE MICE SIMULATIONS

The set of large N-body simulations described in this paper were carried out on the Marenostrum supercomputer at the Barcelona Supercomputing Center (<http://www.bsc.es>), hence their acronym MICE (Marenostrum-Instituto de Ciencias del Espacio).

All simulations were ran with the Gadget-2 code (Springel 2005) assuming the same flat concordance LCDM model with parameters $\Omega_m = 0.25$, $\Omega_\Lambda = 0.75$, $\Omega_b = 0.044$, and $h = 0.7$. The linear power spectrum had spectral tilt $n_s = 0.95$ and was normalized to yield $\sigma_8 = 0.8$ at $z = 0$. Special care was taken in order to avoid spurious artifacts from the initial conditions (*transients*). Thus, the initial particle distributions were laid down either using the Zeldovich approximation with a high starting redshift or 2nd order Lagrangian Perturbation Theory (2LPT) (Scoccimarro 1998; Crocce et al. 2006) (see Sec. 4.1 for details).

The main goal of the MICE set is to study the formation and evolution of structure at very large scales, with the aim of simulating with enough mass resolution the size of future large extra-galactic surveys, such as DES (Annis et al. 2005) or PAU (Benitez et al. 2009), and test robustly statistical and possible systematic errors. Fig.1 shows the set of MICE simulations in the mass resolution-volume plane. They sample cosmological volumes comparable to the SDSS main sample ($0.1 h^{-3} \text{Gpc}^3$), the SDSS-LRG survey ($1 h^{-3} \text{Gpc}^3$), PAU or DES ($9 h^{-3} \text{Gpc}^3$), and those of huge future surveys such as EUCLID ($\sim 100 h^{-3} \text{Gpc}^3$), in combination with mass resolutions from $3 \times 10^{12} h^{-1} M_\odot$

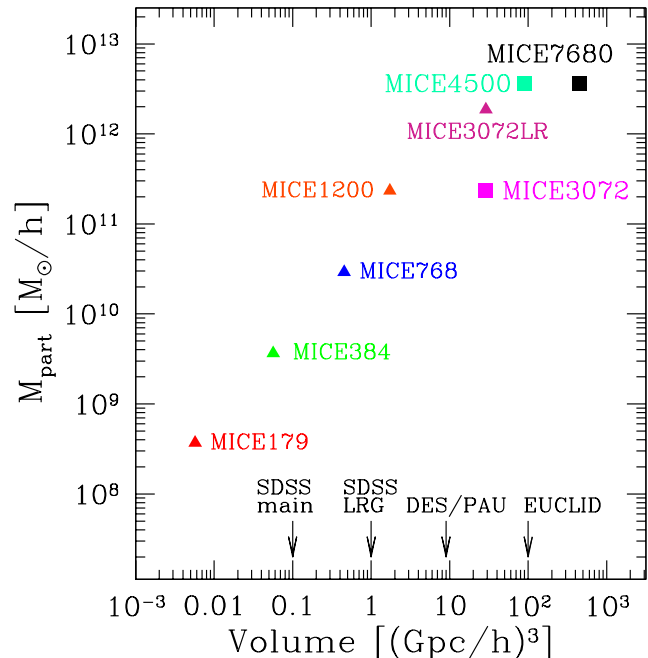


Figure 1. *The MICE simulations in the mass resolution-volume plane:* they span over volumes comparable to the SDSS-main sample ($0.1 h^{-3} \text{Gpc}^3$), SDSS-LRG survey ($1 h^{-3} \text{Gpc}^3$), DES or PAU surveys ($9 h^{-3} \text{Gpc}^3$), and up to huge volumes such as the planned EUCLID mission ($100 h^{-3} \text{Gpc}^3$), and deliver mass resolutions from $3 \times 10^{12} h^{-1} M_\odot$ down to $3 \times 10^8 h^{-1} M_\odot$. In turn, the largest volume simulations (big squares) map the mass function at the high-mass end, $\sim 10^{15} h^{-1} M_\odot$, whereas the test simulations (small triangles) extend the dynamic range down to halos of $10^{10} h^{-1} M_\odot$.

down to $3 \times 10^8 h^{-1} M_\odot$. In turn, the largest volume simulations (squares) map the mass function at the high-mass end, $\sim 10^{15} h^{-1} M_\odot$, whereas the test simulations (triangles) extend the dynamic range down to halos of $10^{10} h^{-1} M_\odot$. Table 1 summarizes the identifying parameters of the main MICE simulations.

Notice that for one particular case (MICE1200) we implemented a set of 20 independent realizations, in order to compare statistical errors on different quantities obtained from an strictly “ensemble error” approach from other internal or external error estimates.

In addition to the production of comoving outputs at several redshifts, we have constructed projected density and weak lensing maps as well as ligh-cone outputs from the main MICE runs. The mass projected and lensing catalogues were discussed in (Fosalba et al. 2008), while the light-cone catalogue will be presented in future work. Note that both represent a huge compression factor (~ 1000), that may turn essential in dealing with very large number of particles as in our case. Further details and publicly available data can be found at <http://www.ice.cat/mice>.

Run	N_{part}	$L_{\text{box}}/h^{-1} \text{ Mpc}$	$m_p/h^{-1} M_{\odot}$	$l_{\text{soft}}/h^{-1} \text{ Kpc}$	IC	z_i
MICE7680	2048 ³	7680	3.66×10^{12}	50	ZA	150
MICE3072	2048 ³	3072	2.34×10^{11}	50	ZA	50
MICE4500	1200 ³	4500	3.66×10^{12}	100	2LPT	50
MICE3072LR*	1024 ³	3072	1.87×10^{12}	50	ZA	50
MICE768*	1024 ³	768	2.93×10^{10}	50	2LPT	50
MICE384*	1024 ³	384	3.66×10^9	50	2LPT	50
MICE179*	1024 ³	179	3.70×10^8	50	2LPT	50
MICE1200* ($\times 20$)	800 ³	1200	2.34×10^{11}	50	ZA	50

Table 1. Description of the MICE N-body simulations. N_{part} denotes number of particles, L_{box} is the box-size, m_p gives the particle mass, l_{soft} is the softening length, *IC* is the type of initial conditions (Zeldovich Approximation, ZA, or 2nd order Lagrangian Perturbation Theory, 2LPT), and z_{in} is the initial redshift of the simulation. Their cosmological parameters were kept constant throughout the runs (see text for details), the initial global time-step is of order 1% of the Hubble time (i.e, $d \log a = 0.01$, being a the scale factor), and the number of global timesteps to complete the run $N_{\text{steps}} \gtrsim 2000$ in all cases. We ran an ensemble of 20 different realizations with the parameters of MICE1200 primarily to calibrate error estimators. We mark with * those runs that were done for completeness or testing as main purpose.

3 THE HALO MASS FUNCTION

The very large simulated volume spanned by the MICE set allow us to study accurately not only Milky Way size halos, but specially the most massive and rarest halos formed by hierarchical clustering. To this end we built dark matter halo catalogues at each snapshot of interest according to the Friends-of-Friends (FoF) algorithm (Davis et al. 1985) with linking length parameter b set in units of the mean inter-particle distance in each simulation. We will refer to halos defined in this way as FoF(b). For the most part we will deal with the $b = 0.2$ catalogues, although we have also implemented $b = 0.164$ for a first validation of our simulations against the Hubble Volume Simulation (HVS) (Jenkins et al. 2001; Evrard et al. 2002). The HVS is one of the very few publicly available halo catalogue comparable in simulated volume to MICE.

The halo finder algorithm was implemented using the FOF code publicly available at the N-body Shop (<http://www-hpcc.astro.washington.edu/>), with some additional modifications needed in order to handle the large number of particles in reasonable amount of time. The resulting halo catalogues contain not only the mass, position and velocity of the center of mass, and virial velocity, but also information of all the particles forming each halo.

As an example of the size of our outputs we mention that MICE3072 contains at $z = 0$ a total of about 25 million halos more massive than $3.9 \times 10^{12} h^{-1} M_{\odot}$ if the minimum number of particles per halo is set to 20. The most massive object weighs $5.27 \times 10^{15} h^{-1} M_{\odot}$ and is made of 22,561 particles. In turn, MICE7680 contains about 15 million halos with mass greater than $7.3 \times 10^{13} h^{-1} M_{\odot}$, with the biggest reaching $8.4 \times 10^{15} h^{-1} M_{\odot}$.

3.1 Theoretical Predictions

Let us start by recalling some well known results regarding the abundance of halos. The differential mass function is defined as,

$$f(\sigma, z) = \frac{M}{\rho_b} \frac{dn(M, z)}{d \ln \sigma^{-1}(M, z)} \quad (1)$$

where $n(M, z)$ is the comoving number density of halos with mass M and $\sigma(M, z)$ is the variance of the linear density field smoothed with a top hat filter of radius R and enclosing an average mass $M = \rho_b 4\pi R^3/3$,

$$\sigma^2(M, z) = \frac{D^2(z)}{2\pi^2} \int k^2 P(k) W^2(kR) dk, \quad (2)$$

with

$$W(x) = \frac{3}{(x)^3} [\sin(x) - x \cos(x)].$$

In Eq. (2), $D(z)$ is the linear growth factor between $z = 0$ and the redshift of interest, and $P(k)$ the linear power spectrum of fluctuations at $z = 0$.

In Eq. (1) we have explicitly assumed that all the cosmology dependence of the differential mass function enters through the amplitude of linear fluctuations, Eq. (2), at the mass scale M . If the redshift dependence also satisfies this condition the halo abundance as defined by Eq. (1) is said to be universal (Press & Schechter 1974; Sheth & Tormen 1999; Jenkins et al. 2001).

Several analytical derivations (Press & Schechter 1974; Bond et al. 1991; Sheth et al. 2001) or fits (Sheth & Tormen 1999; Jenkins et al. 2001; White 2002; Reed et al. 2003; Reed et al. 2006; Warren et al. 2006; Tinker et al. 2008) have been provided in the literature over the past years, starting from the original Press-Schechter formalism in 1974 (Press & Schechter 1974). In our work we will refer only to the Sheth and Tormen (ST) fit given by (Sheth & Tormen

1999),

$$f_{\text{ST}}(\sigma) = A \sqrt{\frac{2q}{\pi}} \frac{\delta_c}{\sigma} \left[1 + \left(\frac{\sigma^2}{q\delta_c^2} \right)^p \right] \exp \left[-\frac{q\delta_c^2}{2\sigma^2} \right], \quad (3)$$

with $A = 0.3222$, $q = 0.707$ and $p = 0.3$. In addition we will take the value of the linear over-density at collapse as $\delta_c = 1.686$, and ignore its weak dependence on cosmology (Lacey & Cole 1993; Jenkins et al. 2001). The subsequent Jenkins fit (Jenkins et al. 2001),

$$f_{\text{Jenkins}}(\sigma) = A \exp \left[-|\log \sigma^{-1} + b|^c \right], \quad (4)$$

with $A = 0.315$, $b = 0.61$ and $c = 3.8$ corresponding to FoF(0.2) halos, that was obtained at redshifts $z = 0 - 5$ over the range $-1.2 \leq \ln \sigma^{-1} \leq 1.05$. For our cosmology this corresponds to masses $(0.96 \times 10^{10} - 4.0 \times 10^{15}) h^{-1} M_\odot$. Alternatively, we will refer to his fit for FoF(0.164) halos for which $A = 0.301$, $b = 0.64$ and $c = 3.88$ (Eq. B2 in Jenkins et al. 2001). This is valid over the mass range $(8.7 \times 10^{10} - 3.4 \times 10^{15}) h^{-1} M_\odot$ in our cosmology.

More recently Warren et al. 2006 performed a detailed mass function analysis using a set of nested-volume simulations and provided the following values for the best-fit parameters of a ST-like mass function,

$$f_{\text{Warren}}(\sigma) = A \left[\sigma^{-a} + b \right] \exp \left[-\frac{c}{\sigma^2} \right], \quad (5)$$

with $A = 0.7234$, $a = 1.625$, $b = 0.2538$, $c = 1.1982$, obtained from a fit to the mass range $(10^{10} - 10^{15}) h^{-1} M_\odot$ at $z = 0$. We will use Eq. (5) as our bench-mark reference fit.

3.2 The binned Mass Function

In order to compare the predictions for the differential mass function in Eq. (1) with the observed halo abundance in a simulation of volume L_{box}^3 one would measure the number of halos ΔN in a given mass-bin $[M_1 - M_2]$ of width ΔM and characteristic mass M , and define,

$$\frac{dn}{d \ln M} = \frac{M}{L_{\text{box}}^3} \frac{\Delta N}{\Delta M} \quad (6)$$

that is then related to the differential mass function in Eq. (1) after multiplying by the prefactor $-\sigma/\sigma' \rho_b$. However for the most part we will directly compare the number density of halos in a given mass bin with the prediction binned in the same way as the measurements. That is, from Eq. (1) we obtain the theoretical number density of objects per unit mass dn/dm , which is then integrated as,

$$n_{\text{bin}} = \int_{M_1}^{M_2} \left(\frac{dn}{dm} \right) dM = \int_{M_1}^{M_2} \frac{-\rho_b}{M} \frac{1}{\sigma} \frac{d\sigma}{dM} f(M, z) dM \quad (7)$$

to predict $\Delta N/V$. The corresponding value of the mass of the bin is obtained as

$$M_{\text{bin}} = \int_{M_1}^{M_2} \left(\frac{dn}{dm} \right) M dM \quad (8)$$

from the theory and as a mass weighted average, $M = \sum_{\text{bin}} M_i / \Delta N$, from the simulation. Throughout our study we used mass bins equally spaced in log-mass, with $\Delta \log_{10} M / (h^{-1} M_\odot) = 0.1$. We have tested that our conclusions do not depend on this particular choice.

3.3 Comparison with previous work

As a first validation of our set of large volume simulations we compared the halo abundance in MICE3072 to that in the Hubble Volume Simulation (HVS) (Jenkins et al. 2001; Evrard et al. 2002), since they both simulate almost the same total volume. The HVS is among the biggest simulated volume with halo data publicly available², at <http://www.mpa-garching.mpg.de/Virgo/hubble.html>.

We used the catalogue corresponding to a Λ -CDM cosmology and FoF halos with linking length parameter $b = 0.164$ (Jenkins et al. 2001). Thus, in what follows we will refer to the MICE catalogues for this value of b . Finally, for this comparison we employed the low resolution run of MICE3072 (MICE3072LR, see Table 1) that has a similar mass resolution to that in the HVS.

Figure 2 shows the ratio of the mass functions measured in the HVS and MICE3072LR at $z = 0$. The higher abundance of massive halos in the HVS is due mainly to its larger value of σ_8 , equal to 0.9 against 0.8 in MICE. Therefore we include in the figure the expected value for this ratio as predicted by the Jenkins fit in Eq. (4) (or Eq. B2 in Jenkins et al. 2001). The difference between the measured ratio and the prediction are within the claimed accuracy for the Jenkins fit (10 – 15 %). Nonetheless notice that the HVS has a rather late start $z_i = 34$ that leads to an artificially lower abundance (see Tinker et al. 2008 for a discussion on this). If one corrects for this effect, the ratio of data-points in Fig. 2 increases by about 5% at $10^{15} h^{-1} M_\odot$ explaining part of the difference. We thus conclude that for matching volume (and particle mass) our MICE run agrees with the HVS.

4 SYSTEMATIC EFFECTS

Measurements of the high-mass end of the halo mass function are potentially affected by a number of systematics. Below we investigate in detail the most relevant ones: the impact of the choice of initial conditions, discrete sampling of the halo mass profile and mass resolution effects.

4.1 Transients from initial conditions

Several potential sources of systematic errors must be considered and controlled when implementing an N-body run, with their relevance sometimes dictated by the regime at which one is interested (see Lukic et al. 2007 for a detailed analysis). We have performed convergence test regarding force and mass resolution, initial time stepping, finite volume effects, and more. But of particular relevance to the

² We do not include a comparison to the recently available data from the Horizon run (Kim et al. 2008) because of potential systematic issues in that simulation that are expected to affect the abundance of the most massive halos in a substantial manner, such as a low starting redshift $z_i = 23$ combined with the ZA (as discussed in Sec. 4.1). Besides, this simulation uses a rather large force softening length $f_\epsilon = 160 h^{-1} \text{ kpc}$ and low number of global time-steps, $N_{\text{steps}} = 400$.

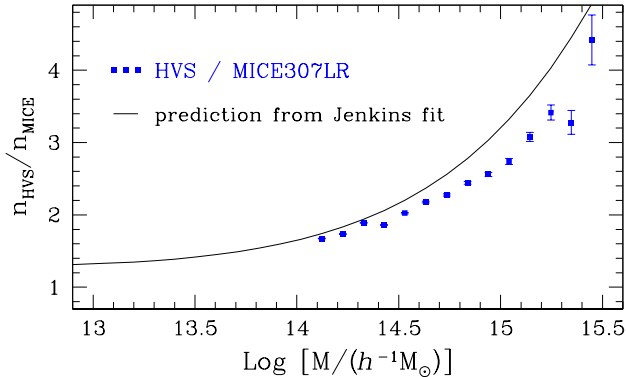


Figure 2. *Comparison to the Hubble Volume Simulation (HVS):* We show results for the FoF halo mass functions at $z = 0$ for a linking length parameter $b = 0.164$ for the HVS in ratio with our low resolution run of MICE3072 (see the MICE3072LR entry in Table 1). We note that both runs have a similar volume and particle mass, but they simulate different cosmologies (mainly a lower σ_8 for MICE3072LR). The solid line corresponds to the prediction for this ratio using the Jenkins fit for FoF(0.164) in Eq. (4). The difference between symbols and the prediction is within the accuracy claimed for the Jenkins fit. In all cases we show only halos with no less than 50 particles, and Poisson errors.

abundance of the largest halos at a given output is the initial redshift and the approximate dynamics used to set the initial conditions and start the run (Scoccimarro 1998; Crocce et al. 2006; Tinker et al. 2008; Knebe et al. 2009).

The generally adopted way to render the initial mass distribution is to displace the particles from a regular grid or a glass mesh, using the linear order solution to the equations of motion in Lagrangian Space. This is known as Zelovich approximation (ZA). Particle trajectories within the ZA follow straight lines towards the regions of high initial overdensity. The ZA correctly describes the linear growth of density and velocity fields in Eulerian Space but, failing to account for tidal gravitational forces that bend trajectories, underestimates the formation of non-linear structure. To leading order this can be incorporated using the second order solution in Lagrangian Perturbation Theory (2LPT) effectively reducing the time it takes for the correct gravitational evolution to establish itself (known as *transients*) once the N-body started. During the period where transients are present the abundance of the most massive objects, that originate from the highest density peaks, is systematically underestimated.

In Crocce et al. 2006 it is shown that transients affect the $z = 0$ mass function reducing it by 5% at $10^{15} h^{-1} M_{\odot}$ if ZA, as opposed to 2LPT, is used to start at $z_i = 49$. This value rises to 10% for $M > 2 \times 10^{14} h^{-1} M_{\odot}$ at $z = 1$. Also Tinker et al. 2008 finds evidence for transients in the HOT runs introduced in Warren et al. 2006 and the HVS (Jenkins et al. 2001). These runs were started in the redshift range $z = 24$ to 35 using ZA. However their own run with $z_i = 60$ is in good agreement with the 2LPT predicted abundance from Crocce et al. 2006 by $z = 1.25$. The impact of the

starting redshift in the high redshift mass function has been investigated in Lukic et al. 2007; Reed et al. 2006; Reed et al. 2003.

To test the significance of transients ourselves we implemented two runs of MICE1200 ($L_{\text{box}} = 1200 h^{-1} \text{Mpc}$ and 800^3 particles) using ZA and 2LPT, both with $z_i = 50$, and the same initial random phases (not listed in Table 1). Figure 3 shows the ratio of the measured mass functions, $n_{\text{ZA}}/n_{\text{2LPT}}$, at $z = 0$ (top panel), $z = 0.5$ (middle) and $z = 1$ (bottom). Top and bottom panels show in addition the results obtained by Crocce et al. 2006 for the same combination of $[z, z_i]$ with a solid line. The dash line in the middle panel corresponds to a simple 2nd order polynomial fit to the ratio at $z = 0.5$. Our results agree very well with those in Crocce et al. 2006 despite the difference in cosmology of the N-body runs (most notably σ_8), confirming an underestimation of the halo abundance by $\sim 5\%$ at $M \sim 10^{15}$, 3.16×10^{14} and $10^{14} h^{-1} M_{\odot}$ at $z = 0, 0.5$ and 1 respectively (and larger for larger masses, at fixed redshift) if ZA $z_i = 50$ is used instead of starting at higher redshift or using 2LPT.

In line with the results above, almost all our runs in Table 1 were started using 2LPT at $z_i = 50$ to avoid transients in the low-redshift outputs. The convergence of 2LPT with $z_i \sim 50$ is discussed in detail in Crocce et al. 2006. For MICE7680 we implemented ZA at high starting redshift ($z_i = 150$) to minimize transients. In this case the convergence is assured by the results in Fig. 6, where its halo abundance is compared with the one in MICE4500, that was started with 2LPT at $z_i = 50$ with completely different random phases (particle load and volume are different). The measured abundance is practically indistinguishable. The only run expected to be affected by transients was MICE3072 that uses ZA at $z_i = 50$. In what follows we will therefore correct the mass function measured in MICE3072 by a simple fit to the ratios shown in Fig. 3.

4.2 FoF Mass Correction

As noted by Warren et al. 2006 the mass of halos determined using the FoF algorithm suffer from a systematic overestimation due to the statistical noise associated with sampling the mass density field of each halo with a finite number of particles. By systematically sub-sampling an N-body simulation and studying the associated FoF(0.2) halo abundance (keeping the linking length parameter fixed) Warren et al. 2006 determined an empirical correction of the mass bias that depends solely in the number of particles n_p composing the halo through the simple expression,

$$n_p^{\text{corr}} = n_p(1 - n_p^{-0.6}). \quad (9)$$

However, as remarked by Lukic et al. 2007, the correction should be checked in a case-by-case basis since it is not the result of a general derivation (see also Tinker et al. 2008). While it is true that for well sampled halos the correction is relatively small (e.g. 2.5% for halos with 500 particles) the impact that a few percent correction to the mass has in the halo abundance can be large is one refers to the most massive halos living in the rapidly changing high-mass tail of the mass function, as we are investigating in this paper.

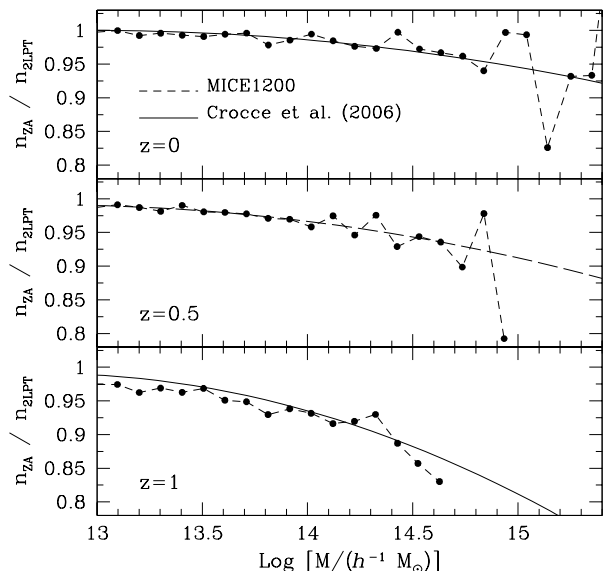


Figure 3. *Transients in the mass function:* ratio of mass functions measured at $z = 0$ (top panel), $z = 0.5$ (middle) and $z = 1$ (bottom), for N-body runs similar to MICE1200 (see Table 1) started at $z_i = 50$ using either ZA or 2LPT to set-up the initial conditions. The solid line at $z = 0, 1$ panels displays the result of a comparable work done by Croce & Scoccimarro (2006), but for a different cosmology and mass resolution. Middle panel shows a 2nd order polynomial fit to the ratio n_{2LPT}/n_{ZA} . Clearly, the approximate dynamics and starting redshift used to set-up initial condition plays a substantial role in the abundance of the rarest halos.

For this reason we have carried out an independent check of the correction in Eq. (9), with particular emphasis in the regime $M > 10^{13-14} h^{-1} M_{\odot}$, where the mass function is exponentially suppressed.

We randomly sub-sampled *every* simulation in the MICE set to several degrees (1 every $n = 2, 4$ and 8 particles) and run the FoF algorithm afterwards keeping the linking length parameter $b = 0.2$ fixed (i.e. with the link length $n^{1/3}$ larger in each case). Results are shown in Fig. 4 for two representative cases, MICE768 and MICE7680, but they extrapolate to all others in Table 1.

The correction in Eq. (9) is able to bring the sub-sampled mass functions into agreement with the original fully sampled one over the whole dynamic range (up to $4 \times 10^{15} h^{-1} M_{\odot}$). Most notably in the case of MICE7680 whose particle mass and volume makes it sample the mass function exponential tail with low Poisson shot-noise but with halos of no more than ~ 2300 particles, what makes it very sensible to such mass corrections. Finally, we have also tested that varying the factor 0.6 leads to worse matching.

Hence, in what follows we will refer to the abundance of *mass corrected* FoF halos, unless otherwise stated.

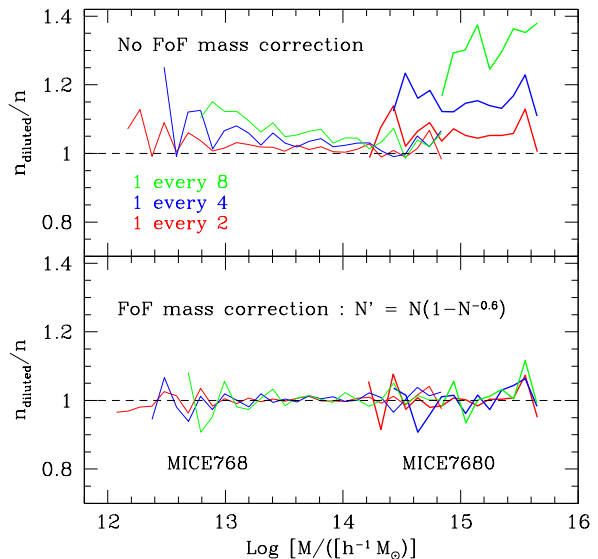


Figure 4. *FoF Mass Correction:* We tested the correction to the systematic mass over-estimation intrinsic to the FoF algorithm (Warren et al. (2006)) in all of our dynamic range, but with particular emphasis at the very high-mass end (i.e. using MICE7680 and MICE4500). We randomly selected one every n particles ($n = 2, 4, 8$ in red, blue and green respectively) and ran the FoF algorithm afterwards with a linking length $n^{1/3}$ larger. The figure shows the corresponding ratio to the fully sampled mass function before (top panel) and after (bottom) the correction, for the cases of MICE7680 and 768. Notably, in all of our simulations the simple expression in Eq. (9) brings the full and sub-sampled mass functions into agreement.

4.3 Mass Resolution Effects

For a first glimpse of the abundance of massive objects in MICE, we display in Fig. 5 the mass function of FoF(0.164) halos obtained from our largest runs (in terms of simulated volume), including the corrections for mass and abundance discussed above in Secs. (4.1,4.2).

MICE3072 (blue squares) is in good agreement with the Jenkins prediction over more than two decades in mass, overlapping with the results from the larger MICE7680 (green circles) and MICE4500 (red triangles) for M in $10^{14-15} h^{-1} M_{\odot}$

However, as we transit towards the high-mass end ($M \gtrsim 10^{15} h^{-1} M_{\odot}$) the abundance in the grand sampling volume of MICE7680 rises over the one in MICE3072 (and HVS) reaching a 20% difference. In addition, measurements in MICE4500 (red triangles) are in very good agreement with those in MICE7680 even though these runs correspond to completely different initial conditions, softening length, box-size, etc (see Table 1).

We recall that MICE7680 and MICE4500 have roughly the same mass resolution to that in the HVS, but a volume 16.7 and 3.4 times larger, respectively. In turn, MICE3072 has roughly the box-size of the HVS, but 8 times better mass resolution.

To check that the “excess” abundance at large masses in

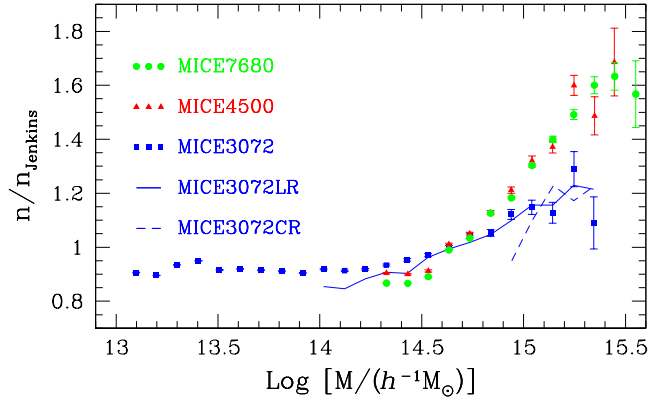


Figure 5. *Mass Resolution effects on the high-mass end:* We show the abundance of FoF(0.164) halos at $z = 0$ in MICE3072 in blue squares, MICE4500 in red triangles and MICE7680 in green circles. We find a systematic rise over the Jenkins prediction for $M \gtrsim 10^{15} h^{-1} M_{\odot}$. The *low-resolution* simulation MICE3072LR (solid line) and the *very-low resolution* simulation MICE3072CR (dashed line) evidence that our results are robust to mass resolution effects at large masses.

not an artifact due to poor mass resolution we have included in Fig. (5) the mass function measured in MICE3072LR and in a *very-low* mass resolution run not listed in Table 1 ($L_{\text{box}} = 3072 h^{-1} \text{Mpc}$, $N_p = 512$, and $m_p = 1.5 \times 10^{13} h^{-1} M_{\odot}$). They both agree remarkably well with MICE3072 at $M \gtrsim 10^{15} h^{-1} M_{\odot}$, showing that the abundance we found using MICE7680 and MICE4500 is robust to mass resolution effects, once the Warren et al. 2006 correction is taken into account.

In summary, we have tested the robustness of our results in front of several possible systematic effects. Early starting redshifts or inappropriate initial dynamics can affect the high-end mass function at the several % level. Hence the MICE simulations used either the 2LPT dynamics, or ZA with high-starting redshift ($z \sim 150$), with the exception of MICE3072 whose mass function we nonetheless correct as described in Sec. 4.1. In addition halo masses were computed using the correction of Warren et al. 2006, that we independently tested focusing in the regime of very massive halos, in order to avoid a bias towards higher masses at low particle number. Lastly, we studied whether the rather high particle mass of MICE7680 and MICE4500 can impact the abundance of massive halos by implementing a set of runs with fixed (large) volume and decreasing mass-resolution. The abundance of massive halos in these runs are in very good agreement once the Warren et al. 2006 correction is considered, reinforcing the robustness of our mass function measurements in front of mass resolution effects.

5 THE ABUNDANCE OF FOF(0.2) HALOS

Let us now turn to the mass function measurements in our catalogues of FoF(0.2) halos. Figure 6 shows the measured

mass function in the MICE simulations tabulated in Table 1. We display the ratios to the Sheth & Tormen fit in Eq. (3), binned in the same way as the measurements. Top panel corresponds to masses corrected for the FoF(0.2) bias as described in Warren et al. 2006 and discussed in Sec. 4.2, Eq. (9). Bottom panel contains un-corrected mass functions. In both panels the solid line represents the Warren fit given in Eq. (5), while dashed corresponds to Jenkins fit in Eq. (4). The corrected mass functions agree very well with the Warren fit, but only up to $10^{14} h^{-1} M_{\odot}$. Past that mass there is a systematic underestimation of the halo abundance in MICE768 and MICE3072 that reaches 20% at $M \sim 5 \times 10^{14} h^{-1} M_{\odot}$ (notice that we show only points with relative Poisson error $\leq 5\%$). Part of this effect can be attributed to transients in the simulations used by Warren et al. 2006 to calibrate the high-mass end, as discussed in (Crocce et al. 2006; Tinker et al. 2008).

For larger masses, $M \gtrsim M^{15} h^{-1} M_{\odot}$, the underestimation of the Warren fit is even more severe, and grows monotonously with M . This in part might be due to volume effects: the abundance of halos at the high-mass end is expected to be extremely low, of order $n_{\text{halo}}/h^{-3} \text{Mpc}^3 \lesssim 10^{-7}$ ($z = 0$), 10^{-8} ($z = 0.5$), and 10^{-9} ($z = 1$) at $10^{15} h^{-1} M_{\odot}$ (integrated over mass bins of $\Delta \log_{10} M = 0.1$). This means that already at moderate redshifts, $z = 0.5$, a simulation of $L_{\text{box}} = 3 h^{-1} \text{Gpc}$ will contain only about 300 halos and therefore measuring the abundance of halos will be the subject to large uncertainties, i.e. the expected (shot-noise) error will be already of order 6%. By including larger volume simulations, such as MICE4500 ($L_{\text{box}} = 4.5 h^{-1} \text{Gpc}$) and MICE7680 ($L_{\text{box}} = 7.68 h^{-1} \text{Gpc}$), we are able to increase the number of halos by up to a factor ~ 16 , thus decreasing the associated halo abundance uncertainties by a factor of ~ 4 . As shown in Fig.6 (top panel) results from both large volume simulations (MICE4500 & MICE7680) agree very well in the high-mass end ($M \gtrsim 3 \times 10^{14} h^{-1} M_{\odot}$). This agreement serves as a validation test for the implementation of each of them as well as for the high-mass end result, given that these two simulations share the same particle mass but have different initial dynamics (2LPT vs. ZA) and random phases.

6 ERROR ESTIMATION

In a rather general sense the most common source of statistical error considered in theoretical studies of halo abundance is solely the shot-noise contribution (e.g. Reed et al. 2006; Warren et al. 2006; Lukic et al. 2007; Jenkins et al. 2001). The importance of considering sample variance in addition to Poisson shot-noise had been highlighted in (Hu & Kravtsov 2002), where it is shown that it can not be neglected in front of shot-noise for deriving precise cosmological constraints. Following this criteria, Tinker et al. 2008 recently used jack-knife errors with the intention to account for both sampling variance at low mass and Poisson shot-noise at high ones.

To deepen into these considerations we will dedicate this section to perform a detailed study of different methods

to estimate the error or variance in mass function measurements. One particular goal is to obtain well calibrated errors in order to implement an accurate fit that could improve the high-mass description of Eq. (5).

We will pay particular attention in comparing how internal errors (i.e. those derived using only the N-body for which the mean mass functions is measured, such as jack-knife) perform against external ones and theoretical predictions, depending on the mass regime and total simulated volume under consideration.

One of the *internal* methods that we implemented is Jack-knife re-sampling (Zehavi et al. 2005). For this we divided the simulation volume under consideration into N_{JK} non-overlapping regions, and computed the halo number density in the full volume omitting one of these regions at a time. The variance (defined as the relative error squared) in the i -bin of the number density is then obtained as,

$$\sigma_{JK}^{(i)2} = \frac{1}{\bar{n}^{(i)2}} \frac{N_{JK} - 1}{N_{JK}} \sum_{j=1}^{N_{JK}} (n_j^{(i)} - \bar{n}^{(i)})^2 \quad (10)$$

where $\bar{n}^{(i)}$ is the mean number density of halos for that bin. In what follows we will show results using $N_{JK} = 5^3$, but we have checked that the estimates have already converged with varying N_{JK} .

Another *internal* method we considered was to assume that the halos are randomly sampled and form a Poisson realization of the underlying number density field. In this case,

$$\sigma_{Poisson}^{(i)2} = 1/N_i \quad (11)$$

where N_i is the number of halos in the i mass bin.

For estimating the variance *externally* in a volume V , we used an N-body of volume V_L , with $V_L \gg V$. We then divide V_L into several non-overlapping regions of volume V and measure the number density in each sub-volume. This method, which we refer to as *sub-volumes*, is similar in spirit to boost-trap sampling except that the sub-volumes are not thrown at random and do not overlap. Thus, this method has the advantage of incorporating the effect of long-wavelength modes which are absent in the volume V .

For example, for mass function errors in MICE179 we divided MICE384 in 8 sub-volumes and MICE768 in 80 sub-volumes. In this way, the best statistics for the error is achieved at the mid-to-high mass regime of MICE179 because the mass resolution of MICE768 does not allow to test all the way down to $M \sim 3.16 \times 10^{11} h^{-1} M_\odot$ (although MICE384 does). Nonetheless both MICE384 and MICE768 leads to a very consistent error estimation in MICE179 for its whole dynamic range, showing no dependence on mass resolution. For MICE384 we divided MICE768 in 8 sub-volumes and MICE3072 in 512 sub-volumes. The rest of box-sizes follow this same logic, that is, their variance in the mean number density was obtained from analyzing the next-in-volume runs as listed in Table 1.

Our last *external* method is ensemble average. This we can only apply to one box-size, $L_{box} = 1200 h^{-1}$ Mpc, using the ensemble of 20 independent realizations of MICE1200 as listed in Table 1.

Finally, to derive a theoretical estimate of the variance in the measured mass function consider fluctuations in the mean number density of halos of a given mass, $\bar{n}_h(M)$, as coming from two different sources (see Hu & Kravtsov 2002 for the original derivation). Firstly, a term arising from fluctuations in the underlying mass density field δ_m , if we consider the halo number density to be a tracer of the mass. If this relation is simply linear and local then $\delta n_h(M, \mathbf{x})/\bar{n}_h = b(M)\delta_m(\mathbf{x})$, where b is the halo bias.

Secondly, a shot-noise contribution δn_{sn} due to the imperfectness of sampling these fluctuations with a finite number of objects. This noise satisfies $\langle \delta n_{sn} \rangle = 0$ and is assumed to be un-correlated with δ_m . Furthermore, if we assume the halo sample to be a Poisson realization of the true number density this error becomes a simple Poisson white-noise with variance $\langle \delta n_{sn}^2 \rangle / \bar{n}_h^2 = 1/\bar{n}_h V = 1/N$, where N is the total number of objects sampled within the volume V . Within these assumptions we then have,

$$\delta n_h(M, \mathbf{x}) = b(M)\bar{n}_h(M)\delta_m(\mathbf{x}) + \delta n_{sn}. \quad (12)$$

The number density of objects of this mass within the simulation is estimated by,

$$n = \int_V d^3x W(\mathbf{x}) [\bar{n}_h + \delta n_h], \quad (13)$$

where $W(\mathbf{x})$ is the simulation window function, normalized such that $\int_V d^3x W(x) = 1$. The variance of the number density measurements in the simulation is then given by,

$$\begin{aligned} \langle n^2 \rangle - \bar{n}_h^2 &= \frac{\bar{n}_h}{V} + b^2 \bar{n}_h^2 \int d^3x_i \int d^3x_j W(\mathbf{x}_i) W(\mathbf{x}_j) \\ &\quad \times \langle \delta_m(\mathbf{x}_i) \delta_m(\mathbf{x}_j) \rangle, \end{aligned} \quad (14)$$

and can be cast as,

$$\sigma_h^2 = \frac{\langle n^2 \rangle - \bar{n}_h^2}{\bar{n}_h^2} = \frac{1}{\bar{n}_h V} + b_h^2 \int \frac{d^3k}{(2\pi)^3} |W(kR)|^2 P(k), \quad (15)$$

where $P(k)$ is the linear power spectrum of mass. For simplicity, we will assume the simulation window function W to be top-hat in real space, Eq. (3), with smoothing radius such that the window volume equals the simulated one, i. e. $R = (3V/4\pi)^{1/3}$.

The first term in Eq. (14) is the usual shot-noise contribution to the variance, that we introduced rather *had-hoc* in Eq. (12), but it can also be derived in the context of the halo model as the contribution from the 1-halo term (Takada & Bridle 2007). The second term, know as sampling variance, is the error introduced by trying to estimate the true number density using a finite volume.

As discussed in Sec. 3.2 one is in practice interested in the halo abundance within bins of mass range $[M_1 - M_2]$ and characteristic mass M . Thus in Eq. (15) we will compute M and \bar{n}_h from Eqs. (7,8) and the bias as,

$$b_h = \frac{1}{\bar{n}_h} \int_{M_1}^{M_2} b_{ST}(M) (dn/dm) dM, \quad (16)$$

where b_{ST} is the prediction for the linear bias dependence on halo mass from Sheth & Tormen 1999,

$$b_{ST}(M) = 1 + \frac{q\delta_c^2/\sigma^2 - 1}{\delta_c} + \frac{2p/\delta_c}{1 + (q\delta_c^2/\sigma^2)^p}, \quad (17)$$

with parameters $q = 0.707$ and $p = 0.3$ and $\sigma = \sigma(M)$ given in Eq. (2). Equation (17) follows from considering variations of the unconditional mass function in Eq. (3) with respect to the critical over-density for collapse δ_c . Thus, strictly speaking this bias expression should be weighted by dn/dm from Eq. (3) when integrating Eq. (16) (Sheth & Tormen 1999; Manera et al. 2009). However we have found that using a fit to the MICE mass function instead leads to better agreement with measurements of clustering in the simulations. Accordingly we will use this fit also to estimate M and \bar{n}_h , entering in Eq. (15).

Figure 7 shows the result of our *external*, *internal* and *theoretical* error study. Clearly the Poisson shot-noise dominates the error budget for $M \gtrsim 10^{14} h^{-1} M_\odot$ corresponding to $\sigma_{MF}/MF > 5\%$ (and $\log \sigma^{-1} \lesssim 0.06$). At smaller masses the sampling variance becomes increasingly important rapidly dominating the total error (this is more so for smaller box-sizes). Jack-knife re-sampling does capture this trend but only partially, in particular for the smaller box-sizes ($\lesssim 500 h^{-1} \text{Mpc}$) where sampling variance from the absence of long-wavelength modes is more significant. This seems to indicate that the jack-knife regions must have a minimum volume (e.g. while jack-knife works well at $10^{13} h^{-1} M_\odot$ in MICE768, it does not for MICE179 at the same mass). This is an important result to consider in further studies where jack-knife re-sampling is used to improve upon Poisson shot-noise. The total error can be underestimated by a factor of a few, e.g. 3 (1.5) at $10^{12} h^{-1} M_\odot$ (10^{13}) in MICE179.

On the other hand, the theoretical error from Eq. (15) is in remarkably good agreement with the sub-volumes method described above across all box-sizes (not shown in MICE7680 and MICE3072 panels of Fig. 7 because is indistinguishable from the other estimates). This can be taken as a cross-validation of these two methods.

In addition we have tested how these different methods compare with the ensemble error in the mass function obtained from the 20 independent runs of MICE1200. For the sub-volumes estimation we divided MICE7680 in 264 regions of volume almost identical to that of MICE1200 (as well as MICE3072 in 18 regions for consistency checks). The result is that, for $L_{box} = 1200 h^{-1} \text{Mpc}$, the sub-volume error is larger than the ensemble one by a factor of about 20% at $M \sim [10^{13} - 3.16 \times 10^{14}] h^{-1} M_\odot$. The reason is that each sub-volume region ‘‘suffers’’ fluctuations in the mean density caused by the long-wavelength modes present in the larger box-size from which they have been obtained (MICE7680 or MICE3072 in this case). These modes, that introduce an extra-variance, are absent in each of the ensemble members that satisfy periodic boundary conditions at the scale $L_{box} = 1200 h^{-1} \text{Mpc}$. Thus, the ensemble error (from running different simulations) does not always work well because it can suffer from volume effects.

This conclusion can be nicely reinforced using Eq. (15), that performs very well here also. One can mimic the absence of long-wavelength modes by setting the low- k limit in the sampling variance integral in Eq(15) to be the fundamental mode of MICE1200 ($k_f = 2\pi/1200 h \text{Mpc}^{-1}$). In this case the theoretical model agrees with the ensemble error (in fact,

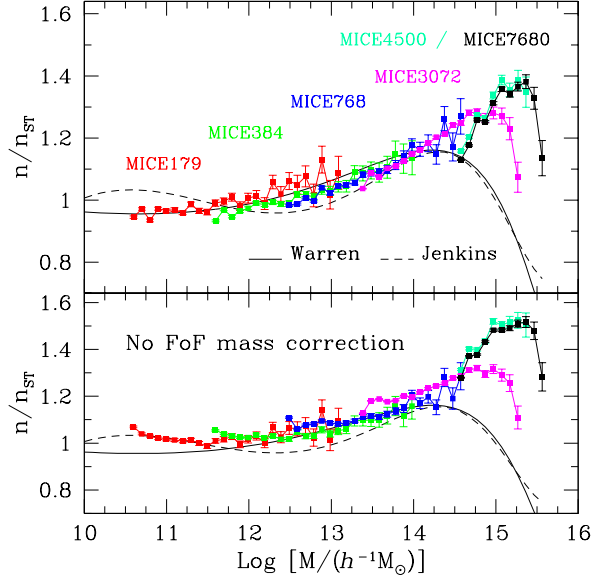


Figure 6. The MICE *mass function* at $z=0$, measured after combining data from the set of MICE simulations with box-sizes $L_{box} = 179, 384, 768, 3072, 4500$ and $7680 h^{-1} \text{Mpc}$ (in red, green blue, magenta, sea-green and black respectively) and varying mass resolutions (see Table 1 for further details). Top panel corresponds to the FoF mass as described in Warren et al. (2006). In the bottom panel we do not include this correction. In both figures we display the ratio to the Sheth and Tormen (1999) prediction and include the corresponding Warren and Jenkins fits for reference (solid and dashed lines). In each case the low-mass end is set by requiring a minimum of 100 particles per halo while the high-mass by requiring a relative error below 5% (displayed error bars correspond to Poisson shot-noise).

σ_h turns to be mostly dominated by shot-noise). Instead, by setting it to $k_f \sim 0$ one recovers the sub-volumes estimate.

In summary, the sub-volume method should be considered as the one comprising all statistical uncertainties: shot-noise, sampling variance and volume effects (the fact that there are fluctuations in scales larger than the sample size). The theoretical estimate in Eq. (15) is consistent with it to a remarkably good level, for the masses and box-sizes tested in this paper. Hence, is a powerful tool for studies involving the abundance of massive halos (Roza et al. 2009; Vikhlinin et al. 2009).

7 THE FITTING FUNCTION FOR THE ABUNDANCE OF MASSIVE HALOS

The accurate sampling of the mass function requires a demanding combination of very big volumes and good mass resolution. As shown in Fig.1, using the MICE set of simulations we have sampled volumes up to $450 h^{-3} \text{Gpc}^3$ with a wide range of mass resolutions yielding a dynamic range $10^8 < M/(h^{-1} M_\odot) < 10^{12}$ in particle mass (see also Table 1).

As shown in Fig. 6, the ST and Warren fits underpredict

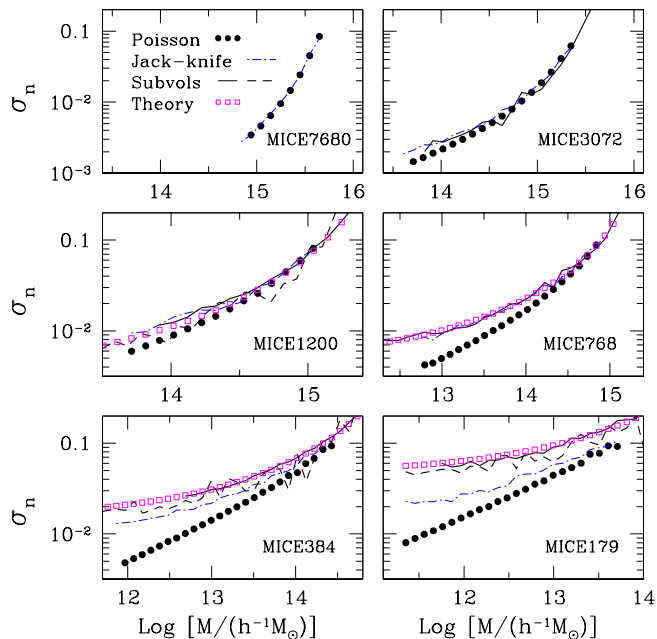


Figure 7. *Sampling variance vs. shot-noise:* The panels show different estimates for the variance in the halo mass function within each of the 6 box-sizes used throughout this paper. Dot symbols correspond to Poisson shot-noise and is only shown for halos with a minimum of 200 particles and until the relative error reaches 10% (as used in Sec. 7). Dot-dashed blue line is the result of implementing jack-knife re-sampling in the given box-size. Solid and dashed black lines are the sub-volumes method described in the text that uses independent sub-divisions of larger-size boxes. For this method we include cases in which two larger volume runs are used (panels of MICE179, MICE384 and MICE1200). Empty magenta squares are the theoretical estimate in Eq. (15) that includes both sampling and shot-noise variance. The variance is shot-noise dominated roughly for $M > 10^{14} h^{-1} M_{\odot}$ (depending on the box-size). While jack-knife does capture some sampling variance at smaller masses, it is not fully satisfactory. It can under-estimated the error by a factor of 2 – 3 at $10^{12} h^{-1} M_{\odot}$. Notably, the sub-volumes and theoretical estimates are in very good agreement across all box-sizes and full mass range.

the abundance of the most massive halos found in our N-body simulations for $M > 10^{14} h^{-1} M_{\odot}$, although Warren gives accurate results for lower masses.

In this section we derive new fits based on the MICE set of simulations, sampling the mass function over more than 5 orders of magnitude in mass, and covering the redshift evolution up to $z = 1$. For this purpose we use a set of MICE simulations with increasing volume and corresponding decreasing mass resolution, in order to sample the mass range from the power-law behavior at low masses, $M \sim 10^{10} h^{-1} M_{\odot}$ and up to the exponential cut-off at the high-mass end. As discussed in Sec. 5, the abundance of halos at the high-mass end is expected to be extremely low, of order $n_{halo}/h^{-3} \text{Mpc}^3 \lesssim 10^{-7}$ ($z = 0$), 10^{-8} ($z = 0.5$), and 10^{-9} ($z = 1$) at $10^{15} h^{-1} M_{\odot}$ (integrated over mass bins of $\Delta \log_{10} M = 0.1$), and thus we shall use MICE4500

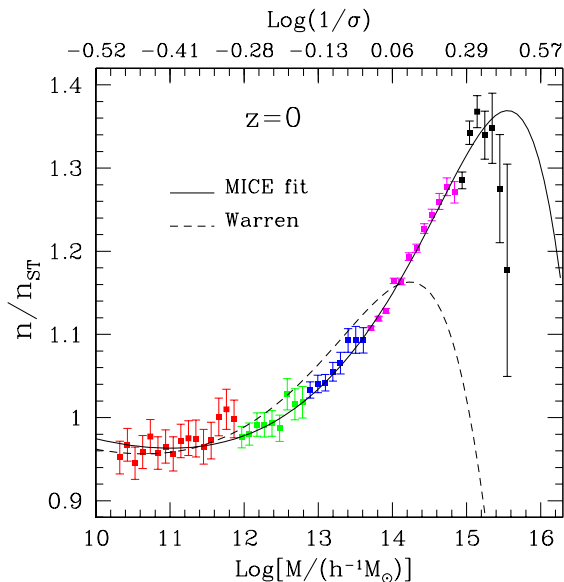


Figure 8. *Mass function fit at $z=0$.* Symbols as in Fig. 6. Measurements sample the mass function over more than 5 orders of magnitude, $4 \times 10^{15} > M/h^{-1} M_{\odot} > 2 \times 10^{10}$. Results are ratioed to the ST fit. The best-fit to the N-body measurements (“MICE” fit, solid line) is given by the Warren-like mass function, Eq (5), with parameters as given in Table 2. The fit agrees with N-body data to 2% accuracy in practically all the dynamic range ($2.5 \times 10^{15} > M/h^{-1} M_{\odot} > 2 \times 10^{10}$). The Warren fit (dashed line) matches the N-body to 3% accuracy in the low mass end $M/h^{-1} M_{\odot} < 10^{14}$, but it significantly underestimates the abundance of the most massive halos: we find a 10% (25%) underestimate at $M/h^{-1} M_{\odot} \sim 3 \times 10^{14}$ (10^{15}), and larger biases for more massive objects.

($L_{box} = 4.5 h^{-1} \text{Gpc}$) and MICE7680 ($L_{box} = 7.68 h^{-1} \text{Gpc}$) in order to get a more accurate measurement of the halo abundance in this regime. In practice, we shall combine cluster counts from both simulations to get a more robust estimate. As it will be shown below, our fitting functions recover the measured mass function over the entire dynamic range and its redshift evolution with $\sim 2\%$ accuracy.

For our fitting procedure we use the following simulations: MICE179,384, 768, 3072, 4500 and MICE7680 (see Fig.1 and Table1) and match them so that in overlapping mass bins we shall adopt the abundance estimated from the simulation with the lower associated error, provided halos include a minimum of 200 particles, except for the smallest box-size simulation, MICE179, for which we use down to 50 particle halos. This is done in order to sample small enough halos (as small as $10^{10} h^{-1} M_{\odot}$) whose abundance has been accurately measured in previous analyses (see e.g, Warren et al. 2006; Tinker et al. 2008) and that we aim at recovering as well with our fitting functions.

On the other hand, for $M \gtrsim 3 \times 10^{14}$ we average results from both MICE4500 and MICE7680. As shown above, for $z = 0$, results for $M > 10^{15} h^{-1} M_{\odot}$ from MICE7680 are found to be in full agreement with those of MICE4500 despite the different initial conditions and time-step size used,

z	A	a	b	c	χ^2/ν
0	0.58	1.37	0.30	1.036	1.25
0.5	0.55	1.29	0.29	1.026	1.20

Table 2. Mass function best-fit parameters for $f(\sigma, z)$, Eq. (5), and goodness of fit.

what provides a robustness test to our measurements at the highest mass bins.

The fit to the mass function is then determined using a diagonal χ^2 analysis,

$$\chi^2 = \sum_{i=1}^N \frac{(n_{fit}^{(i)} - n_{Nbody}^{(i)})^2}{\sigma^{(i)2}} \quad (18)$$

where $n_{fit}^{(i)}$ ($n_{Nbody}^{(i)}$) is the theoretical (N-body) mass function integrated over the i -th logarithmic mass bin of width $\Delta \log_{10} M / (h^{-1} M_{\odot}) = 0.1$, and the errors $\sigma^{(i)}$ are computed using the Jack-knife (JK) estimator. The JK estimator is consistent with theoretical errors and sub-volumes dispersion (see Fig. 7), except for the smallest mass bins (sampled by MICE179, see lower right panel in Fig. 7) for which the JK errors significantly underestimate other error estimates. By using JK errors for those bins we just give them a larger statistical weight in the χ^2 analysis, thus making sure the fit recovers the expected low mass behavior (i.e. we assume something similar to a *low-mass prior*).

We summarize the fitting results for the MICE mass functions at $z = 0$ and 0.5 in Table 2. The best-fit to the N-body measurements at $z = 0$ (“MICE” fit, solid line) is given by the Warren-like mass function, Eq. (5), with parameters $A = 0.58$, $a = 1.37$, $b = 0.30$, $c = 1.036$ with $\chi^2/\nu = 1.25$. As shown in Fig. 8, the fit recovers our N-body data to 2% accuracy in practically all the dynamic range, that is, for $2.5 \times 10^{15} > M / (h^{-1} M_{\odot}) > 4 \times 10^{10}$. The Warren fit (dashed line) matches the N-body to the same accuracy in the mass regime $M < 10^{14} h^{-1} M_{\odot}$, but significantly underestimates the abundance of the most massive halos: we find a 10% (30%) underestimate at $M = 3.16 \times 10^{14} h^{-1} M_{\odot}$ ($10^{15} h^{-1} M_{\odot}$). This can be attributed in part to transients in the (Warren et al. 2006) N-body data, as discussed in Sec. 5.

At higher-redshifts, the mass function deviates from the universal form in Eq. (5), and the fitting parameters change accordingly. In particular, for $z = 0.5$ we find the best-fit values $A = 0.55$, $a = 1.29$, $b = 0.29$, $c = 1.026$, yielding a $\chi^2/\nu = 1.20$. As seen in Fig. 9 (left panel), this fit recovers the N-body measurements to 2% accuracy in all the dynamic range (i.e., for $10^{15} > M / (h^{-1} M_{\odot}) > 2 \times 10^{10}$). The MICE fit at $z = 0$ extrapolated with the linear growth to $z = 0.5$ ($z = 1$) overestimates the measurements by 3–6% (10%) as the halo mass increases. This in turn shows to what extent the FoF(0.2) mass function deviates from universality.

8 HALO GROWTH FUNCTION

In the previous section we found that the mass function deviates significantly from universality (or self-similarity). Here we investigate in detail the *halo growth function*, i.e. the evolution of the halo abundance with redshift, using the scaling evolution of the best-fit parameters as a starting point.

The evolution of the fitting function parameters with redshift, as shown in Fig. 9, indicate that the FoF(0.2) mass function, at least for the linking length $l = 0.2$, is non-universal at the 5%–10% level in the red-shift range tested. This is in agreement with previous studies (Jenkins et al. 2001; Reed et al. 2003; Reed et al. 2006; Lukic et al. 2007; Tinker et al. 2008) but is consistently extended here to the high-mass regime, hard to sample robustly particularly at higher red-shifts.

To account for this evolution we next try to fit the mass function growth with a simple ansatz. If we follow (Tinker et al. 2008) and assume that the fitting parameters are a simple function of the scale factor, $a = 1/(1+z)$, we can model the evolution as,

$$P(z) = P(0)(1+z)^{-\alpha_i}; P = \{A, a, b, c\}; \alpha_i = \{\alpha_1, \dots, \alpha_4\} \quad (19)$$

where $P(0)$ are the fitting parameters at $z = 0$, as given by Table 2. Therefore, we can use the lowest redshift measurements at $z = 0$ and $z = 0.5$ to determine the slope parameters α_i ,

$$\alpha_1 = 0.13, \alpha_2 = 0.15, \alpha_3 = 0.084, \alpha_4 = 0.024. \quad (20)$$

If the ansatz is correct, i.e. the growth of the mass function can be modeled to a good approximation with Eq. (19), one should be able to *predict* the measured cluster evolution at higher redshifts. Using the values of α_i as given above, we *predict* the following fitting parameters at $z = 1$: $A = 0.53$, $a = 1.24$, $b = 0.28$, $c = 1.019$, what gives a good match to simulations, $\chi^2/\nu = 1.92$. As shown in both panels of Fig. 9, the scaling ansatz recovers the measured mass function to 3% accuracy in most of the dynamic range (i.e. for $3.16 \times 10^{14} > M / (h^{-1} M_{\odot}) > 2 \times 10^{10}$).

We conclude from this that the ansatz Eq. (19) can be safely used to make predictions about the abundance of the most massive halos at intermediate redshifts.

It has been argued by (Tinker et al. 2008) that the non-universality of the mass function is basically a consequence of the evolution of the halo concentrations, which in turn is mostly due to the change of the matter density Ω_m with redshift and thus $f(\sigma)$ should be rather modeled as a function of the linear growth rate of density perturbations, $D(z)$. In order to test this hypothesis, we have repeated the analysis where the scaling of $f(\sigma)$ is parametrized as follows,

$$P(z) = P(0)(D(z)/D(0))^{\beta_i}; \beta_i = \{\beta_1, \dots, \beta_4\} \quad (21)$$

In this case the slope parameters are found to be, $\beta_1 = 0.22$, $\beta_2 = 0.25$, $\beta_3 = 0.14$, $\beta_4 = 0.04$. Using this model we estimate $f(\sigma)$ parameters at $z = 1$ to be, $A = 0.52$, $a = 1.22$, $b = 0.28$, $c = 1.017$, what provides a slightly worse fit to the N-body measurements, with $\chi^2/\nu = 2.85$. Therefore, we find some evidence in favor of a scaling ansatz based on the scale factor with respect to that based on the growth rate.

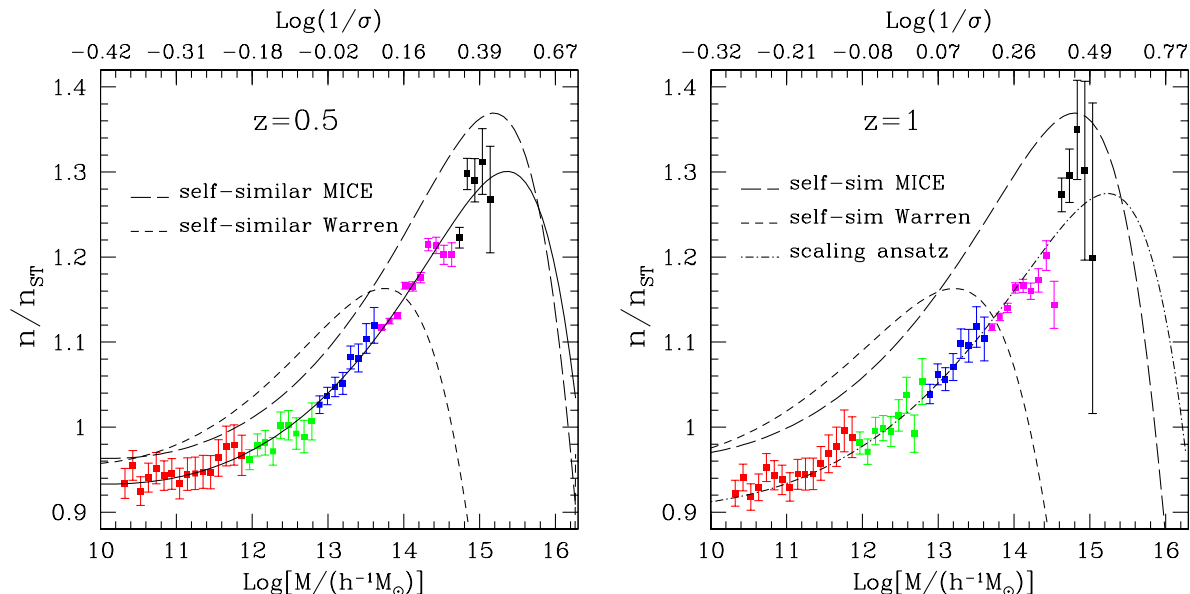


Figure 9. *Left:* Mass function fit at $z=0.5$. The best-fit to the N-body measurements is given by Eq. (5) with parameters as given in Table 2 (solid line). This fit matches simulations to 2% accuracy in all the dynamic range ($3 \times 10^{14} > M/h^{-1} M_{\odot} > 2 \times 10^{10}$). Assuming a *self-similar* form of the mass function (i.e., using the N-Body fit at $z=0$ extrapolated with the linear growth to $z=0.5$), one overestimates the measurements by 3–6% as the halo mass increases (see dashed line). The (self-similar) Warren fit yields an even larger overestimate of the halo abundance (3–10%). This shows to what extent the FoF(0.2) mass function deviates from universality. *Right:* Mass function fit at $z=1$. Growth of the mass function with redshift can be accurately modeled with a simple ansatz, Eqs.(19),(20),(22) (see discussion below, in Sec.8), and it provides a good fit to simulations. We find that deviations from universality of the halo abundance increase with redshift: the self-similar MICE fit exceed by up to 10% the simulation measurements (and similarly for the Warren fit).

We note that our analysis is of limited validity since we have only considered one cosmology and one should explore a wider parameter space to draw stronger conclusions on this point.

In summary, the fit to the FoF(0.2) halo mass function measured in the MICE simulations between redshift 0 and 1 is given by,

$$f_{\text{MICE}}(\sigma, z) = A(z) \left[\sigma^{-a(z)} + b(z) \right] \exp \left[-\frac{c(z)}{\sigma^2} \right] \quad (22)$$

with $A(z) = 0.58(1+z)^{-0.13}$, $a(z) = 1.37(1+z)^{-0.15}$, $b(z) = 0.3(1+z)^{-0.084}$, $c(z) = 1.036(1+z)^{-0.024}$.

We can now explore how the *halo growth function* evolves in more detail. For this purpose, we study the halo mass function integrated in wider logarithmic bins ($\Delta \log_{10} M/(h^{-1} M_{\odot}) = 0.5$), and concentrate on the highest mass bins where we find the largest deviations between our N-body measurements and available fits. Figure 10 (left panel) shows the halo growth factor as measured in several comoving redshifts in the MICE simulations.

Our simulations show that the abundance of massive halos drops by half (one) order of magnitude for the $\log M/(h^{-1} M_{\odot}) = 13.5 - 14$ ($14.5 - 15$) from $z=0$ to $z=1$, in rough agreement with analytic fits. However, as displayed in the right panels of Fig. 10, the (self-similar) ST and Warren fitting functions (see short and long-dashed lines respectively) only match the high-mass end of the measured mass function at $z=0.5$ to 15% accuracy. The Warren fit at $z=1$

underestimates simulation data by up to 30%. On the other hand, using the *predicted* halo abundance growth from the MICE fits at low redshift (red solid line) recovers the measured abundance at $z=1$ to better than 1%. We have used the scaling functions given by Eq. (19), however we have checked that our results do not change significantly if we use the growth rate ansatz instead, Eq. (21).

9 COSMOLOGICAL IMPLICATIONS: BIAS ON DARK-ENERGY CONSTRAINTS

The cluster mass function is one of the standard cosmological probes used by current and proposed surveys to constrain cosmological parameters. In particular, the cluster abundance as a function of cosmic time is a powerful probe to determine the nature of dark-energy. However usage of the cluster abundance as a cosmological probe is limited by systematics in the mass-observable relations and the potential impact of priors (see e.g, Battye & Weller 2003; Weller & Battye 2003).

Here we concentrate on the impact of priors in the mass function on extracting the dark-energy equation of state, w . As shown in 8, the halo mass function measured in simulations deviates from self-similarity by as much as 15%, depending on redshift and halo mass. We shall estimate how this systematic departure from universality can potentially *bias* estimates of w .

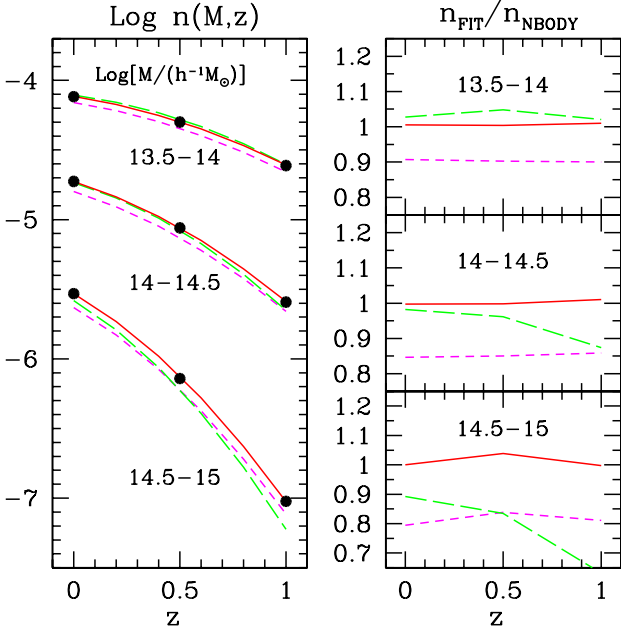


Figure 10. Halo Growth Function: evolution of the halo abundance with redshift. We show the three most massive logarithmic bins (with $\Delta \log M / (h^{-1} M_{\odot}) = 0.5$), where we find the most significant deviations between N-body and available fits. *Left panel:* the abundance of massive halos drops by half (one) order of magnitude for the $\log M / (h^{-1} M_{\odot}) = 13.5 - 14$ ($14.5 - 15$) from $z=0$ to $z=1$, in rough agreement with analytic fits. *Right panel:* Residuals between analytic fits (lines) to N-body measurements (symbols) for the same mass bins (increasing mass from top to bottom panels). ST and Warren fitting functions (short and long-dashed lines respectively) only match the high-mass end of the measured mass function at $z=0.5$ to 15% accuracy. The extrapolated Warren fit to $z=1$ underestimates MICE data by up to 30%. The *predicted* halo abundance growth from the MICE fits at low redshift (red solid line; see text for details) recovers the measured abundance at $z=1$ to better than 1%.

As a working case, we will consider a tomographic survey with photometric accuracy Δz , and estimate the shift in the recovered value of, w , by including cluster counts in redshift shells up to a given depth, z . For simplicity we consider a constant dark-energy equation of state, although this same analysis could be easily extended to a time varying $w(z)$. Since the *wrong prior* on the halo mass function can be mistaken by the *right* cluster abundance for a *different* cosmology, the bias on w , for a given redshift, will be determined by the relative sensitivity on w of the two cluster count probes of dark-energy: the mass function growth and the survey volume up to a given depth.

We perform a χ^2 analysis to determine the bias as a function of survey depth by comparing halo counts in redshift shells as follows,

$$\chi^2 = \sum_{z_i} \frac{(n(w)^{(i)} - n(z)_{Nbody}^{(i)})^2}{\sigma^{(i)2}}, \quad (23)$$

where $n(w)^{(i)}$ are the counts from the assumed *self-similar*

mass function, for a cosmology with a given value of w , integrated from a minimum mass M_{min} up to some maximum mass M_{max} , for the redshift shell z_i of width Δz_i within which we can safely consider the mass function to be independent of z . In turn, $n(z)_{Nbody}$ are the corresponding counts measured in simulations that use the fiducial cosmology with $w = -1$, and that are accurately described by the scaling ansatz, Eq. (22). The associated error is assumed to be pure shot-noise given by the N-Body counts, $\sigma = \sqrt{n_{Nbody}}$. Here we make estimates for full-sky surveys (i.e, we will draw optimistic forecasts for a given survey depth), although smaller areas can be easily incorporated in our analyses by scaling the shot-noise error accordingly. We shall consider surveys with SZ detected clusters, i.e, with a redshift independent mass threshold $M \sim 10^{14} h^{-1} M_{\odot}$, and constant photo-z error $\Delta z = 0.1$. The upper limit in the mass is taken to be $10^{15.5} h^{-1} M_{\odot}$ to avoid possible systematic departures of the N-Body fit used beyond this mass-cut with respect to the simulation measurements. However we have checked our results do not change if we take larger mass cuts.

Figure 11 shows the bias on w as a function of survey depth z for two different priors on self-similar mass functions, the ST fit and the MICE fit (i.e, assuming the fit at $z = 0$ extrapolated to higher- z). We find that the estimated bias is robust to better than 20% to changes in the SZ mass threshold M_{min} from $10^{13.8}$ to $10^{14.2}$ (see dashed lines in Fig.11). For the ST fit, the bias can be as large as 50% for survey depth $z \lesssim 1$, whereas for the MICE self-similar fit it reduces to 20% at most for the same depth. The bias at low- z results from the relatively small and comparable sensitivities to changes in w of the geometric (volume) and the shape of the mass function growth. On the other hand, the strong bias at low- z for the ST prior is due to the poor fit it gives to N-Body for the relevant masses $M \gtrsim 10^{14} h^{-1} M_{\odot}$. This systematic effect tends to decrease for increasing depth as the mass function growth becomes a much stronger function of the dark-energy equation of state than the redshift shell volume (for constant Δz) and thus it determines the cluster counts irrespective of the prior on the mass function. This trend is strengthened by the fact that the shot-noise error per z -shell drops with depth as well (see bottom panel of Fig.11), so the high- z counts down-weight the observed low- z bias on w . Therefore, for deep surveys $z \gtrsim 1$ any bias associated to the mass function tends to be washed out.

10 DISCUSSION AND CONCLUSIONS

The abundance of clusters as a function of cosmic time is a powerful probe of the growth of large scale structure. In particular, clusters provide us with a test of the sensitivity of the growth of structure to cosmological parameters such as the dark-matter and dark-energy density content, its equation of state, or the amplitude of matter density fluctuations. More importantly, the abundance and clustering of clusters are complementary to other large scale structure probes such as the clustering of galaxies, weak lensing and supernovae (see e.g, Hu & Kravtsov 2002; Cunha 2009; Cunha et al. 2009; Estrada et al. 2009).

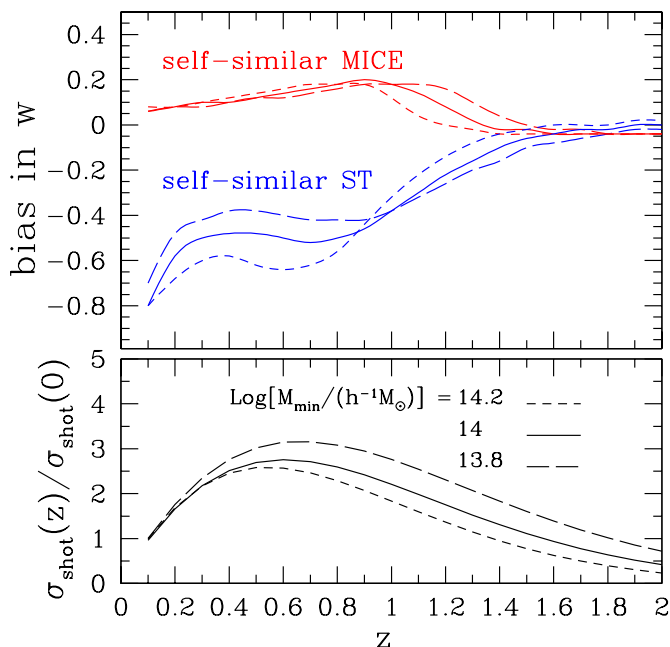


Figure 11. Bias on w induced by self-similar prior on the mass function. *Upper panel:* Assuming the self-similar ST (MICE) fit induces up to 50% (20%) shift in the recovered value of w for shallow or medium depth surveys $z \lesssim 1$, whereas the effect tends to be negligible for deep surveys. *Bottom panel:* the relative shot-noise error decreases with redshift, what makes high- z cluster counts, which are dominated by the strong variation of the mass function with w , to down-weight biases induced by the low- z counts.

In order to plan and optimally exploit the scientific return of upcoming astronomical surveys (e.g. DES, PAU, PanSTARRS, BOSS, WiggleZ, Euclid) one needs to make accurate forecasts of the sensitivity of these probes to cosmological parameters in the presence of systematic effects. Accurate determination of the abundance of clusters is limited by our knowledge of the relation between cluster mass and observable (see e.g. Hu 2003). One key ingredient in this mass-observable calibration is the precise determination of the halo mass function.

In this paper we use a new set of large simulations, including up to $2048^3 \simeq 10^{10}$ particles, called MICE (see Table 1) to accurately determine the abundance of massive halos over 5 orders of magnitude in mass, $M = (10^{10} - 10^{15.5}) h^{-1} M_{\odot}$, and describe its evolution with redshift. Notice that the MICE simulations sample cosmological volumes up to $7.68^3 \simeq 450 h^{-3} \text{Gpc}^3$. Armed with these simulations we estimate, for the first time, the mass function over a volume more than one order of magnitude beyond the Hubble Volume Simulation size, $3^3 = 27 h^{-3} \text{Gpc}^3$ (Jenkins et al. 2001; Evrard et al. 2002). Our results have been tested against mass resolution, choice of initial conditions, and simulation global time-step size.

Our findings can be summarized as follows:

- We confirm previous studies (see Crocce et al. 2006) showing that an accurate determination of the mass function

is sensitive to the way initial conditions are laid out. For a fixed starting redshift, the usage of 2LPT instead of the ZA to set-up the initial conditions helps to avoid the effects of transients that tend to artificially decrease the abundance of large-mass halos. Alternatively, one can use ZA with a high enough starting redshift. In particular, we find an under-estimate of the halo abundance by $\sim 5\%$ at $M \sim 10^{15}$, 3.1×10^{14} and $10^{14} h^{-1} M_{\odot}$ at $z = 0, 0.5$ and 1 respectively (and larger for larger masses, at fixed redshift) if ZA $z_i = 50$ is used instead of 2LPT. All our mass functions were safe from transients or corrected accordingly for those simulations that need it (i.e. MICE3072, see Table 1).

- As highlighted by Warren et al. 2006, the mass of halos determined using the FoF algorithm suffer from a systematic over-estimation due the statistical noise associated with sampling the halo density field with a finite number of particles. The precise form of this correction has to be checked on a case by case basis. We confirm the results of (Warren et al. 2006), particularly testing them for large halo masses, that the mass correction for the FoF(0.2) halos follows Eq. (9).

- For masses $M > 10^{14} h^{-1} M_{\odot}$, we find an excess in the abundance of massive halos with respect to those from the Hubble volume simulation (Jenkins et al. 2001; Evrard et al. 2002), once corrected for the different cosmology used, that is a few times the Poisson error (see Fig.5). As argued in Sec.4.1, we conclude that this difference can be largely explained by systematics due to transients affecting the Hubble volume simulation.

- From an extensive study of error estimates we conclude that: (i) sample variance is significant only for halos of $M < 10^{14} h^{-1} M_{\odot}$, and dominates over shot-noise for box-sizes $L_{box} < 1 h^{-1} \text{Gpc}$. Consistently, Poisson shot-noise errors under-estimate the total error budget by factors $2 - 4$ at $10^{12-13} h^{-1} M_{\odot}$ in these volumes. (ii) Jack-knife re-sampling is in general consistent with external estimators such as ensemble averages, and theoretical errors. However it underestimates the total error budget for small box-sizes ($< 500 h^{-1} \text{Mpc}$) where sampling variance is more important due to the lack of long-wavelength modes and to the fact that jack-knife regions are not independent. (iii) For all our runs the theoretical error estimate in Eq. (15) is in remarkably good agreement with our external *sub-volumes* estimator that incorporates fluctuations due to long-wavelength modes in addition to sampling and shot-noise variance at the scale of the given box-size.

- Existing analytic fits (Sheth & Tormen 1999; Warren et al. 2006), accurately reproduce our N-body measurements at up to $10^{14} h^{-1} M_{\odot}$, but fail to reproduce the abundance of the most massive halos, underestimating the mass function by 10% (30%) at $M = 3.16 \times 10^{14} h^{-1} M_{\odot}$ ($10^{15} h^{-1} M_{\odot}$).

- The FoF halo mass function deviates from universality (or self-similarity). In particular, the Sheth & Tormen (1999) fit, if extrapolated to $z \geq 0$ assuming universality leads to an underestimation of the abundance of 30%, 20% and 15% at $z = 0, 0.5, 1$ for fixed $\nu = \delta_c/\sigma \approx 3$ (corresponding to $M \sim 7 \times 10^{14} h^{-1} M_{\odot}$, $2.5 \times 10^{14} h^{-1} M_{\odot}$ and $8 \times 10^{13} h^{-1} M_{\odot}$ respectively, see Fig. 9). This is due to some extent to the ST not being a very good fit at $z = 0$. If we instead extrapolate our $z = 0$ MICE best fit, we level of evo-

lution in the amplitude of the halo mass function is $\sim 5\%$ (10%) at $z = 0.5$ ($z = 1$).

- We provide a new analytic fit, Eq. (22), that reproduces N-body measurements over more than 5 orders of magnitude in mass, and follows its redshift evolution up to $z = 1$, that is accurate to 2%. The new fit has the functional form of (Warren et al. 2006), but with different parameters to account for the excess in the high mass tail (see also Table 2).

- Systematic effects in the abundance of clusters can strongly bias dark-energy estimates. We estimate that medium depth surveys $z \leq 1$, using SZ cluster detection, could potentially bias the estimated value of the dark-energy equation of state, w , by as much as 50%. This effect is however an upper limit to the amplitude of this systematic effect, and it drops quickly with depth. For deep surveys $z \sim 1.5$, such as DES, the estimated bias is largely negligible.

As discussed in Sec. 1 there are various ways to define halos and their masses, but the most commonly employed algorithms are Friends-of-Friends (FoF) and Spherical-Overdensities (SO). From an observer view-point it is not clear that a single definition is optimal for all kinds of detection techniques (see Voit 2005 for a review). X-rays observations are easier and more robust in the inner center of clusters, that have higher density contrasts and are more relaxed. Hence, it seems clear that spherical apertures are more appropriate in this case, although with threshold density contrasts as high as 500 or more (Vikhlinin et al. 2009). Optical richness is measured within regions of fixed projected physical radius, resembling a modified FoF method. Hence, they demand a proper calibration of the mass-richness relation (Bode et al. 2001) if one does not want to rely on the correlation with the cluster X-ray properties. Cluster detection through the Sunyaev-Zeldovich (SZ) effect are relatively recent in statistical terms and suffers from several other sources of error (e. g. Carlstrom et al. 2002). Yet, both halo definitions have been employed in the literature. For instance, mock SZ maps have been built and exploited using FoF (Schulz & White 2003), and correlations between X-ray properties and the SZ signal were studied starting from SO catalogues (Stanek et al. 2009b).

Our particular work focused on halos defined through the FoF percolation method leaving the SO for a follow-up study. Nonetheless we have tested that the trend seen towards high masses when comparing different MICE runs persist for decreasing linking length, that is, when probing the inner most regions of the halos.

We also leave for future work a more thorough investigation of the cosmological implications of our results. In particular, it remains to be seen what is the impact of the bias on cosmological parameters induced by mass function priors in the presence of other systematic effects such as the uncertainties in the cluster mass-observable relations and the cosmological parameter degeneracies present in cluster abundance measurements.

ACKNOWLEDGMENTS

We would like to thank Jorge Carretero, Gus Evrard, Marc Manera, Sebastián Pueblas, Román Scoccimarro, Volker Springel, and Masahiro Takada for very useful help and discussions at different parts of this project. We acknowledge support from the MareNostrum super-computer (BSC-CNS, www.bsc.es), through grants AECT-2008-1-0009, AECT-2008-2-0011, AECT-2008-3-0010, and Port d'Informació Científica (PIC, www.pic.es) where the simulations were ran and stored, the use of the Friends-of-Friends code from the University of Washington N-body shop (www-hpcc.astro.washington.edu) and the 2LPT code for initial conditions (cosmo.nyu.edu/roman/2LPT). The MICE simulations were implemented using the Gadget-2 code (www.mpa-garching.mpg.de/gadget). Funding for this project was partially provided by the Spanish Ministerio de Ciencia e Innovacion (MICINN), projects 200850I176, AYA2006-06341, Consolider-Ingenio CSD2007-00060, research project 2005SGR00728 from Generalitat de Catalunya and the Juan de la Cierva MEC program.

REFERENCES

- Annis, J. et al., submitted to the Dark Energy Task Force (2005), e-print arXiv:astro-ph/0510195
- Battye, R. A., Weller, J., PRD, **68**, 083506 (2003)
- Benitez, N. et al., ApJ, **691**, 241, (2009)
- Bode, P., Bahcall, N. A., Ford, E. B., Ostriker, J. P., ApJ, **551**, 15 (2001)
- Bond, J. R., Cole, S., Efstathiou, G., Kaiser, N., ApJ, **379**, 440 (1991)
- Boylan-Kolchin, M., Springel, V., White, S. D. M., Jenkins, A., Lemson, G., MNRAS, **398**, 1150 (2009)
- Cabré, A., Gaztañaga, E., MNRAS, **393**, 1183 (2009)
- Cabré, A., Gaztañaga, E., MNRAS, **396**, 1119 (2009)
- Carlstrom, J. E., Holder, G. P., Reese, E. D., ARA&A, **40**, 643 (2002)
- Cohn, J. D., White, M., MNRAS, **385**, 2025 (2008)
- Crocce, M., Pueblas, S., Scoccimarro, R., MNRAS, **373**, 369 (2006)
- Cunha, C., Huterer, D., Frieman, J. A., PRD, **80**, 063532 (2009)
- Cunha, C., PRD, **79**, 063009 (2009)
- Davis, M., Efstathiou, G., Frenk, C., White, S. D. M., ApJ, **292**, 371 (1985)
- Eke, V. R., Baugh, C. M., Cole, S., Frenk, C. S., Navarro, J. F., MNRAS, **370**, 1147 (2006)
- Estrada, J., Sefusatti, E., Frieman, J. A., ApJ, **692**, 265 (2009)
- Evrard, A. E., MacFarland, T. J., Couchman, H. M. P., Colberg, J. M., Yoshida, N., White, S. D. M., Jenkins, A., Frenk, C. S., Pearce, F. R., Peacock, J. A., Thomas, P. A., ApJ, **574**, 7 (2002)
- Fosalba, P., Gaztañaga, E., Castander, F. J., Manera, M., MNRAS, **391**, 435 (2008)
- Frenk, C. S., Colberg, J. M., Couchman, H. M. P., Efstathiou, G., Evrard, A. E., Jenkins, A., MacFarland, T. J., Moore, B., Peacock, J. A., Pearce, F. R., Thomas, P. A., White, S. D. M., Yoshida, N., e-print arXiv:astro-ph/0007362
- Gaztañaga, E., Cabre, A., Castander, F., Crocce, M., Fosalba, P., MNRAS, **399**, 801 (2009)
- Gaztañaga, E., Cabre, A., Hui, L., MNRAS, **399**, 1663 (2009)
- Grossi, M., Dolag, K., Branchini, E., Matarrese, S., Moscardini, L., MNRAS, **382**, 1261 (2007)

- Heitmann, K., Lukic, Z., Habib, S., Ricker, P. M., *ApJ*, **642**, L85 (2006)
- Henry, J. P., Evrard, A. E., Hoekstra, H., Babul, A., Mahdavi, A., *ApJ*, **691**, 1307 (2009)
- Hu, W., *PRD*, **67**, 081304 (2003)
- Hu, W., Kravtsov A. V., *ApJ*, **584**, 702 (2003)
- Jenkins, A.; Frenk, C. S.; White, S. D. M.; Colberg, J. M.; Cole, S.; Evrard, A. E.; Couchman, H. M. P.; Yoshida, N., 2001, *MNRAS*, **321**, 372 (2001)
- Kim, J., Park, C., Gott, R., Dubinski, J., *ApJ*, **701**, 1547 (2009)
- Knebe, A., Wagner, C., Knollmann, S., Diekershoff, T., Krause, F., *MNRAS*, **698**, 266 (2009)
- Lacey, C. G., Cole, S., *MNRAS*, **262**, 627 (1993)
- Lacey, C. G., Cole, S., *MNRAS*, **271**, 676 (1994)
- Lee, J., Shandarin, S. F., *ApJ*, **500**, 14 (1998)
- Lukic, Z., Heitmann, K., Habib, S., Bashinsky, S., Ricker, P. M., *ApJ*, **671**, 1160 (2007)
- Lukic, Z., Reed, D., Habib, S., Heitmann, K., *ApJ*, **692**, 217 (2009)
- Maggiore, M., Riotto, A., e-print arXiv:astro-ph/0903.1251
- Manera, M., Sheth, R. K., Scoccimarro, R., *MNRAS* accepted, e-print arXiv:astro-ph/0906.1314 (2009)
- Mantz, A., Allen, S. W., Ebeling, H., Rapetti, D., *MNRAS*, **387**, 1179 (2008)
- Matarrese, S., Verde, L., Jimenez, R., *ApJ*, **541**, 10 (2000)
- Pillepich, A.; Porciani, C.; Hahn, O., e-print arXiv:astro-ph/0811.4176
- Press, W. H. & Schechter, P., *ApJ*, **187**, 425 (1974)
- Reed, D. S., Bower, R., Frenk, C. S., Jenkins, A., Theuns, T., *MNRAS*, **374**, 2 (2007)
- Reed, D. S., Gardner, J., Quinn, T., Stadel, J., Fardal, J., Lake, G., Governato F., *MNRAS*, **346**, 565 (2003)
- Robertson, B. E., Kravtsov, A. V.; Tinker, J.; Zentner, A. R., *ApJ*, **696**, 636 (2009)
- Rozo, E. et al., e-print arXiv:astro-ph/0902.3702 (2009)
- Schulz, A. E., White, M., *ApJ*, **586**, 723 (2003)
- Scoccimarro, R., *MNRAS*, **299**, 1097 (1998)
- Sheth, R. K. & Tormen, G., *MNRAS*, **308**, 119 (1999)
- Sheth, R. K., Mo, H. J., Tormen, G., *MNRAS*, **323**, 1 (2001)
- Springel, V., *MNRAS*, **364**, 1105 (2005)
- Springel, V., White, S. D. M., Jenkins, A., Frenk, C. S., Yoshida, N., Gao, L., Navarro, J., Thacker, R., Croton, D., Helly, J., Peacock, J. A., Cole, S., Thomas, P., Couchman, H., Evrard, A., Colberg, J., Pearce, F., *Nature*, **435**, 629 (2005)
- Stanek, R., Rudd, D., Evrard, A. E., *MNRAS*, **394**, L11 (2009)
- Stanek, R., Rasia, E., Evrard, A. E., Pearce, F., Gazzola, L., submitted to *ApJ*, e-print arXiv:astro-ph/0910.1599
- Tago, E., Einasto, J., Saar, E., Tempel, E., Einasto, M., Vennik, J., Muller, V., *A&A*, **479**, 927 (2008)
- Takada, M., Bridle, S., *New Journal of Physics*, **9**, 446 (2007)
- Teyssier, R., Pires, S., Prunet, S., Aubert, D., Pichon, C., Amara, A., Benabed, K., Colombi, S., Refregier, A., Starck, J., *Astronomy and Astrophysics*, **497**, 335 (2009)
- Tinker, J., Kravtsov, A. V., Klypin, A., Abazajian, K., Warren, M., Yepes, G., Gottlober, S., Holz, D. E., *ApJ*, **688**, 709 (2008)
- Vikhlinin, A., Kravtsov, A. V., Burenin, R. A., Ebeling, H., Forman, W. R., Hornstrup, A., Jones, C., Murray, S. S., Nagai, D., Quintana, H., Voevodkin, A., *ApJ*, **692**, 1060 (2009)
- Voit, G. M., *Rev. Mod. Phys.*, **77**, 207 (2005)
- Warren, M. S., Abazajian, K., Holz, D. E., Teodoro, L., *ApJ*, **646**, 881 (2006)
- Wen, Z. L., Han, J. L., Liu, F. S., *ApJS*, **183**, 197 (2009)
- Battye, R. A., Weller, J., *New Astron.Rev.*, **47**, 775 (2003)
- White, M., *A&A*, **367**, 27, (2001)
- White, M., *ApJS*, **143**, 241 (2002)
- Zehavi, I. et al., *ApJ*, **630**, 1 (2005)